International Journal of Radiation Oncology biology • physics

www.redjournal.org

Physics Contribution

Automatic Segmentation of the Eye in 3D Magnetic Resonance Imaging: A Novel Statistical Shape Model for Treatment Planning of Retinoblastoma

Carlos Ciller, MSc,[*,†,‡] Sandro I. De Zanet, MSc,[†,§] Michael B. Rüegsegger, PhD,[†,§] Alessia Pica, MD,[‖] Raphael Sznitman, PhD,[†,§] Jean-Philippe Thiran, PhD,[*,¶] Philippe Maeder, MD,[*] Francis L. Munier, MD,[#] Jens H. Kowal, PhD,[†,§] and Meritxell Bach Cuadra, PhD[*,‡,¶]

**Department of Radiology, Lausanne University Hospital and University of Lausanne, Lausanne, Switzerland; [†]Ophthalmic Technology Group, ARTORG Center of the University of Bern, Bern, Switzerland; [‡]Centre d'Imagerie BioMédicale, University of Lausanne, Lausanne, Switzerland; [§]Department of Ophthalmology, Inselspital, Bern University Hospital, Bern, Switzerland; [‖]Department of Radiation Oncology, Inselspital, Bern University Hospital, Bern, Switzerland; [¶]Signal Processing Laboratory, École Polytechnique Fédérale de Lausanne, Lausanne, Switzerland; and [#]Unit of Pediatric Ocular Oncology, Jules Gonin Eye Hospital, Lausanne, Switzerland*

Received Sep 16, 2014, and in revised form Feb 18, 2015. Accepted for publication Feb 25, 2015.

Summary

Diagnosis and treatment of retinoblastoma often requires the laborious task of segmenting the eye anatomy in 3D magnetic resonance images (MRI). Statistical shape modeling (SSM) techniques are successful tools for

Purpose: Proper delineation of ocular anatomy in 3-dimensional (3D) imaging is a big challenge, particularly when developing treatment plans for ocular diseases. Magnetic resonance imaging (MRI) is presently used in clinical practice for diagnosis confirmation and treatment planning for treatment of retinoblastoma in infants, where it serves as a source of information, complementary to the fundus or ultrasonographic imaging. Here we present a framework to fully automatically segment the eye anatomy for MRI based on 3D active shape models (ASM), and we validate the results and present a proof of concept to automatically segment pathological eyes.

Methods and Materials: Manual and automatic segmentation were performed in 24 images of healthy children's eyes (3.29 ± 2.15 years of age). Imaging was performed

Reprint requests to: Carlos Ciller, PhD Candidate, Medical Image Analysis Laboratory, Department of Radiology, Centre Hospitalier Universitaire Vaudois and University of Lausanne, Rue du Bugnon 46, CH-1011 Lausanne, Switzerland. Tel: 41 21 314 75 31 (or) Universität Bern ARTORG Center for Biomedical Engineering Research Ophthalmic Technologies Laboratory, Murtenstrasse 50, CH-3010 Bern, Switzerland; E-mail: carlos.cillerruiz@unil.ch or carlos.ciller@artorg.unibe.ch

This work was supported by Swiss Cancer League grant KFS-2937-02-2012, the Centre d'Imagerie BioMédicale of the University of Lausanne, the École Polytechnique Fédérale de Lausanne; University of Geneva; Centre Hospitalier Universitaire Vaudois, the Hôpitaux Universitaires de Genève; University of Bern, and the Leenaards and Jeantet Foundations.

Conflict of interest: none.

Supplementary material for this article can be found at www.redjournal.org.

Acknowledgments—The authors declare they have no financial relationships relevant to this paper to disclose.

Int J Radiation Oncol Biol Phys, Vol. 92, No. 4, pp. 794–802, 2015
0360-3016/$ - see front matter
http://dx.doi.org/10.1016/j.ijrobp.2015.02.056

modeling anatomical shapes in medical imaging. This work introduces the first fully automatic segmentation of the eye evaluated using MRIs of eyes of 21 children, yielding overlapping measures of 94.90% ± 2.12% for the sclera and cornea, 94.72% ± 1.89% for the vitreous humor, and 85.16% ± 4.91% for the lens.

using a 3-T MRI scanner. The ASM consists of the lens, the vitreous humor, the sclera, and the cornea. The model was fitted by first automatically detecting the position of the eye center, the lens, and the optic nerve, and then aligning the model and fitting it to the patient. We validated our segmentation method by using a leave-one-out cross-validation. The segmentation results were evaluated by measuring the overlap, using the Dice similarity coefficient (DSC) and the mean distance error.

Results: We obtained a DSC of 94.90 ± 2.12% for the sclera and the cornea, 94.72 ± 1.89% for the vitreous humor, and 85.16 ± 4.91% for the lens. The mean distance error was 0.26 ± 0.09 mm. The entire process took 14 seconds on average per eye.

Conclusion: We provide a reliable and accurate tool that enables clinicians to automatically segment the sclera, the cornea, the vitreous humor, and the lens, using MRI. We additionally present a proof of concept for fully automatically segmenting eye pathology. This tool reduces the time needed for eye shape delineation and thus can help clinicians when planning eye treatment and confirming the extent of the tumor.

Introduction

Retinoblastoma is the most common intraocular tumor in children and affects roughly 1 in every 18,000 newborns worldwide (1, 2). With 90% of cases identified by the age of 3, most retinoblastomas are curable, especially when the tumor is confined to the area between the retina and the surface of the vitreous humor (VH) (3). For this reason, accurate and noninvasive techniques that can be used for early diagnosis assessment and tumor extent follow-up or treatment planning are critical.

Today, fundus image photography and 2-dimensional (2D) ultrasonography (US) are the image modalities of choice for the diagnosis and follow-up treatment of intraocular tumors (4). Computed tomography (CT) is often regarded as the superior tool for the detection of intratumoral calcifications within the eye cavity, but it induces ionizing radiation, which has a more negative effect on children than adults. Furthermore, ionizing radiation has been shown to modify the patient's susceptibility to radiation, thus affecting the carriers of the RB1 germline mutation that are responsible for retinoblastoma. Moreover, there is very little evidence regarding the diagnostic accuracy of CT in the context of advanced retinoblastoma (5), and thus, it is less recommended for imaging the disease (3).

Over the last decade, the ophthalmic community has become increasingly interested in magnetic resonance imaging (MRI) (6), mainly due to its favorable tissue contrast and improved image resolution (7). MRI sequences provide a remarkable soft tissue information source, with resolution comparable to the information extracted from CT (8). Additionally, recent studies (3, 9) have provided direct evidence for the usefulness of MRI in both diagnosis and treatment follow-up of retinoblastoma and the fact that the combination of MRI and US would be sufficient to account for all calcifications found using CT. Consequently, quantitative analysis of eye MR images is needed to support the diagnosis and therapy planning with a better and faster eye anatomy delineation. In this context, the existence of a robust and accurate segmentation tool for eye MR images would offer an unprecedented opportunity for multimodal patient-specific eye modeling, that is, combining modalities such as fundus imaging, US with MRI for treatment planning of the eye (8-11).

Until now, the task of segmenting the eye in medical imaging has been completed predominantly by using preestablished sets of parameters. EYEPLAN (12), a framework that estimated the shape of the lens, the cornea, and the sclera, does so by combining parametric spheres. In comparison, OCTOPUS (13), currently widely used in modeling the eye inside CT, applies the same concept but models the eye as combinations of ellipsoids. Both of these methods require an expert to preselect visual landmarks. In addition, these methods have constrained modeling capabilities, because they limit the eye growth patterns as a linear function dependent on the age of the patients. As such, they do not accommodate for a free growth pattern representative of a real eye population. The recent image processing techniques have opened the door to designing more complex models, which enables the segmentation of more regions of interest (ROI) within the eye. In 2006, Singh et al (14) proposed a segmentation method for MRI based on spherical meshes that leveraged the posterior corneal pole and a sphere-modifying parameter. More recently, Cuadra et al (8) designed an algorithm combining parametric active contours with an ellipsoid model, which offered more accurate segmentations of the sclera and the lens on the CT and US images. Despite these advances, the eye treatment planning is far from being optimal.

One key element lacking in the above-mentioned parametric models is the statistical information that can be extracted from the variability of a population. This type of information is offered by statistical shape models

(SSM). These models use a previously trained, constrained model-based algorithm that can account for the deformation of the shape of a structure. Among the SSM, the active shape model (ASM) proposed by Cootes et al (15) is one of the most successful. It has been applied to numerous medical imaging applications (16), mainly to construct automatic segmentation frameworks by using both intensity and shape variation information (17-19). Here, Rüegsegger et al (10) proposed a semiautomated method, requiring minimal user interaction to segment the sclera, the cornea, and the lens on CT images of adult patients (10).

With the aim of providing an accurate method for eye segmentations in MR images, we present an eye model that can capture both the shape variations and the intensity information from a set of the gadolinium-enhanced T1-weighted gradient echo (GE) volumetric interpolated brain examination (VIBE) MR sequences used for retinoblastoma imaging. The proposed 3D MRI ASM is, to the best of our knowledge, the first statistical model of the eye based on MRI data. Importantly, it also involves a fully automatic segmentation of the sclera, the cornea, the lens, and the VH. We evaluated our model using a sample of 24 images of healthy children's eyes and validated it quantitatively by using a leave-one-out cross-validation test. Our experiments show an average Dice similarity coefficient (DSC) of $91.6 \pm 2.20\%$ for the regions of interest (ROIs). In addition, we applied our method to the pathology in 2 patient eyes with retinoblastoma and quantitatively highlighted the benefits of our approach with an average DSC of $93.45 \pm 0.93\%$.

Methods and Materials

Our segmentation procedure can be summarized as follows. We started by constructing an atlas of the eye regions (20). We then extracted an eye point-based shape variation model (PBSVM) and coupled it with the intensity information to build an ASM. Then, to segment a new subject, we followed a 2-step process. First, we automatically found a number of landmarks within the eye to initialize the alignment of the model, and second, we fitted the ASM to the volume. A visual depiction of our framework can be seen in Figure 1.

Training data set and manual segmentation

The dataset used to develop our statistical model is composed of 24 healthy eyes gathered from children 3.29 ± 2.15 years of age (Fig. 2, from 4 months to 8 years, 8 months). All patient information in our study was anonymized and de-identified by physicians prior to our analysis, and the corresponding institution approved the study. MR imaging was performed using a 3-T Verio model (Siemens, Erlangen, Germany) with a 32-channel surface head coil attached. The images were gadolinium-enhanced, T1-weighted VIBE (repetition time/echo time, 20/3.91 ms; flip angle, 12°) (21), and were acquired with 2 different spatial resolutions: $0.416 \times 0.416 \times 0.399$ mm and $0.480 \times 0.480 \times 0.499$ mm. Images included the patient's head, both eyes, and the optic nerves. Images were resampled to a common voxel spacing of $0.416 \times 0.416 \times 0.399$ mm. During imaging, the patients were under general anesthesia (3).

In order to validate our method, an expert radiologist manually segmented all volumes by labeling the sclera, cornea, lens, VH, and optic disc. As described below, an atlas was then created based on the segmented volumes of every patient. Furthermore, axial length, lens size, and width statistics were extracted and compared with the ages of the patients. We observed a strong correlation

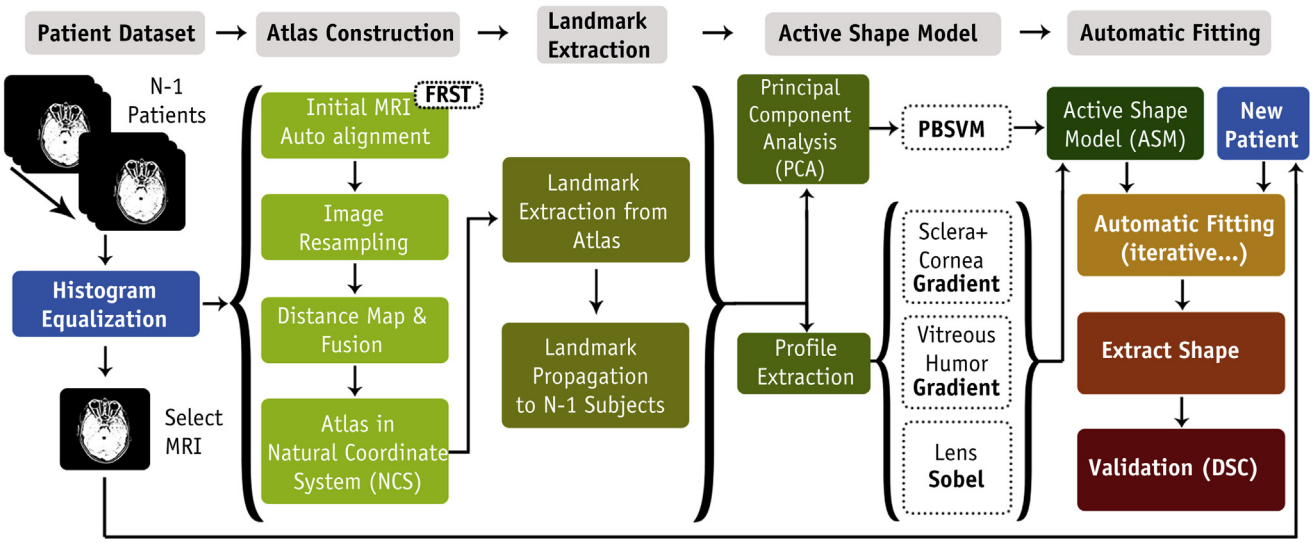

Fig. 1. Diagram represents the fully automatic segmentation framework. We created a model with N-1 patients and tested the performance in the remaining subjects. DSC = Dice similarity coefficient; FRST = fast radial symmetry; MRI = magnetic resonance imaging; PBSVM = point-based shape variation model.

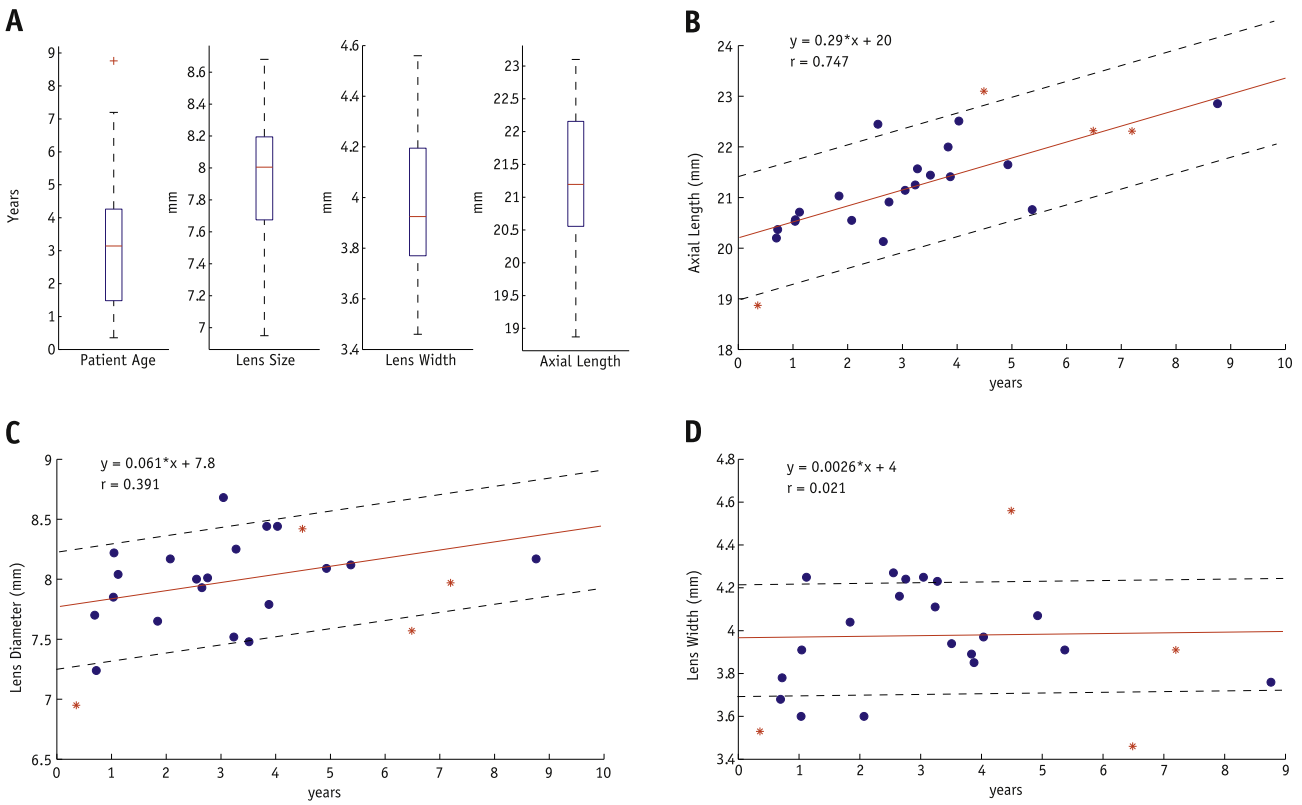

Fig. 2. Patient dataset information. (A) Dataset information distribution. (B) Age versus axial length. (C) Age versus lens size. (D) Age versus lens width. Highlighted values in red are subjects 3, 7, 14, and 15 (Sub03, Sub07, Sub14, and Sub15, respectively). A color version of this figure is available at www.redjournal.org.

between age and axial length (Fig. 2b), as described by Fledelius and Christensen (22), but weak correlations between age and lens size and between age and width (Fig. 2c and d).

For initialization and detection of the eyes, we applied the method proposed by De Zanet et al (23), based on the fast radial symmetry (FRST) algorithm. We automatically detected the center of both eyes in all patients (Fig. 3a), even in the case of enucleation or pathology. Using Digital Imaging and Communications in Medicine (DICOM) format file orientation information, we defined whether it was the left or right eye. This information enabled us to flip the volume over the transversal plane and mirror it for both eyes when required. We then cropped the MRI head volume into 2 smaller volumes of interest (VOIs) of $40 \times 40 \times 40$ mm for both eyes. Next, we retrieved the location of the center of the lens, the optic disc, and the VH (Fig. 3b) (23). These 3 points provided the initial alignment for building the atlas and for fitting a new patient.

Atlas construction

We applied a rigid (ie translation and rotation) preregistration step to the whole patient dataset. Both the center of the VH and the lens were used for translation, and the optic disc position was used for rotation. We then computed the distance map of the manually segmented regions, fused them, and created a baseline atlas. Afterward, we obtained, for each patient, the deformation field (nonrigid free diffeomorphic demons) relative to the baseline atlas (24). Finally, we applied the mean deformation field to the baseline atlas to obtain the atlas in a natural coordinate system (20).

Point-based shape variation model

We represent the surface of the atlas in a natural coordinate system as a point cloud by using a mesh extraction algorithm (25). This was followed by a Gaussian smoothing and a decimation to the regions of the sclera, the cornea, and the VH by 85% and by 10% for the lens. The information loss during the decimation step never induced an error over 0.01 mm on average for all ROIs.

Once the surface was extracted, we warped the atlas back to the patient by using nonrigid diffeomorphic registration (24). The new atlas landmark positions for each subject were then transformed to a tangent space (Eq. 1) to preserve the linearity of the PBSVM, as expressed by Cootes et al (15) in

$$x_t = \frac{|\bar{x}|^2}{x * \bar{x}} \cdot x \qquad (1)$$

where x is the original surface points vector, $\bar{x}$ is the mean overall surface shape, and x_t is the new projection of the

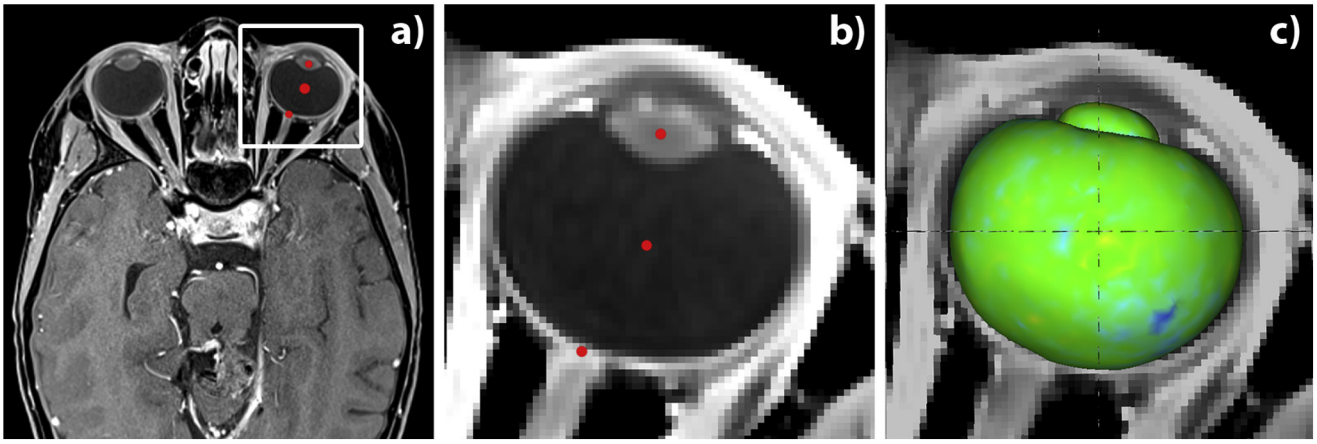

Fig. 3. (a) Magnetic resonance imaging (MRI) volume, highlighting the automatic cropping region and landmark initialization. (b) Preprocessed MRI region of the eye including landmarks (red dots). (c) Segmentation results for the lens and the vitreous humor. A color version of this figure is available at www.redjournal.org.

surface points in the tangent space. The principal component analysis (PCA) (26) of the projection is done to extract the principal components of the point cloud distribution in space. The combined information is known as the shape variation model and is stored in the form of

$$x \approx \bar{x} + \Phi b \tag{2}$$

where $\bar{x}$ is the mean shape, represented as a vector of t points, $\Phi = (\varphi_1|\varphi_2|\ldots|\varphi_t)$ is a matrix which contains the eigenvectors corresponding to the variation of the model at each point, and b is a t-dimensional vector representing the modes of variation. By modifying the b_i value under the constraints $\pm 3\sqrt{\lambda_i}, i = 1..t$, we constrained the model to be within the range of shapes similar to those of the training set. For every position in b, λ is the eigenvalue corresponding to the Φ matrix. We assumed the shape to be represented as a normal distribution of points along shapes $\pm 3\sigma i$ (10, 15, 20).

Active shape model

We connected the PBSVM described in the previous section with the MRI intensity information and created an ASM. In contrast to CT, MRI does not provide fixed intensity values across patients. Therefore, we used the standardization equalization algorithm proposed by Nyul and Udupa (27) to standardize the dataset.

Once the dataset was equalized, we preprocessed the MRI volumes with an anisotropic diffusion gradient filter and windowed the image intensity to highlight the region of the eyeball and lens. We fixed arbitrary common upper and lower thresholds for the windowing and extracted the intensity information at each landmark position. Then, we computed the gradient and Sobel operators along the intensity profiles normal to the surface. Subsequently, we computed the gradient for the sclera/VH and the Sobel for the lens.

We then selected an even distribution of points (28) over the surface of the different regions from the landmark point cloud list (350 points from the sclera-cornea and VH and 300 points for the lens). We extracted the normal surface at these given points and computed the mean gradient intensities or the mean Sobel profiles, as well as the covariance matrices. The length of the extracted profiles depended on the region. We extracted a normalized profile gradient along 11 pixels for the sclera, the cornea, and the VH and 9-pixels-length Sobel profile for the lens.

Automated segmentation

Segmentation of a new patient was carried out as follows. First, the VOI was preprocessed in the same way as the images were processed during the ASM construction; the VOI is not resampled and maintains its original image resolution. We then scanned the profiles normal to the surface of the model. These profiles were compared to the intensity profiles provided by the ASM, and a new matched point is set for each profile along the sampled voxels. The fitting was then reduced to an optimization problem where the Mahalanobis distance to the model shape was minimized (15) by reducing the overall distance between the current shape point and the matched point while constraining the model to be within the deformation range of the PBSVM. In contrast to other work (10), the segmentation scheme that we applied here is 2-fold: first, we fitted the sclera and VH, and then, once the optimum was found, we fit the lens independently (Fig. 3c).

Results

We assessed our segmentation method using a leave-one-out cross-validation test of the ASM. That is, we iterated over each patient, excluding it from the ASM construction

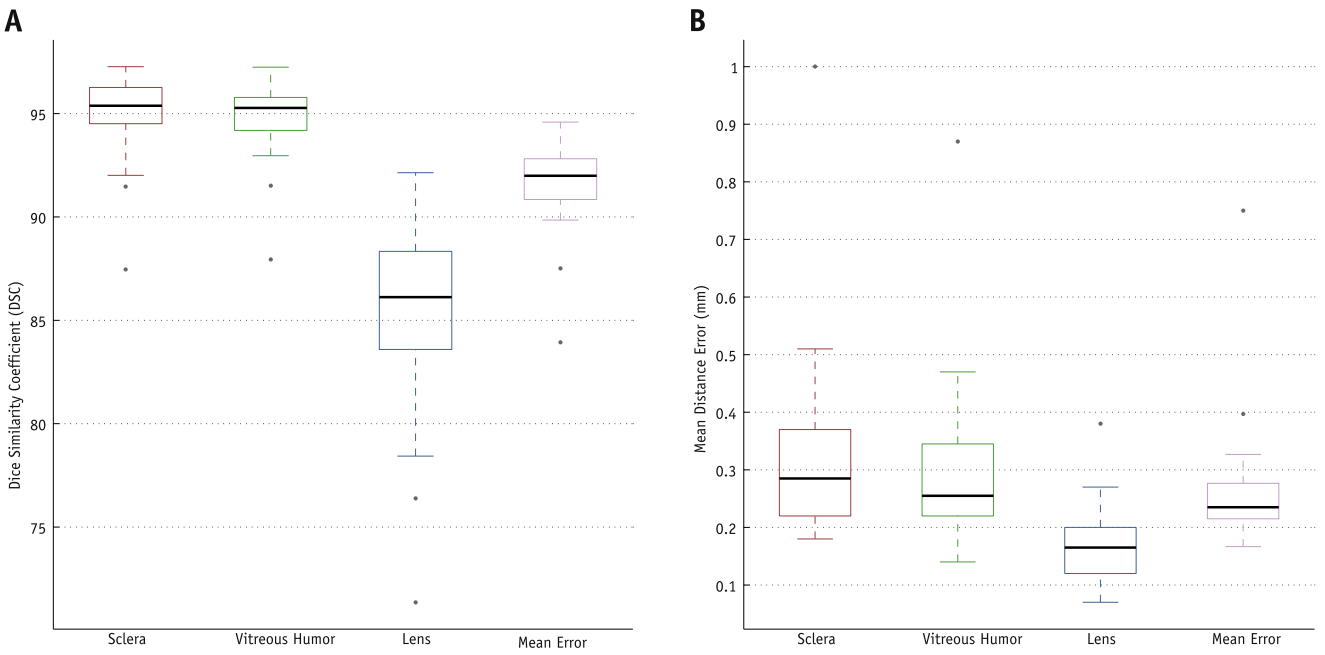

Fig. 4. Leave-one-out cross validation. (A) Mean ± standard deviation Dice similarity coefficient for independent and combined shapes. (B) Mean distance error for every eye region and combined mean error.

and automatically fit the generated model to the excluded patient. The quality of the segmentations were evaluated by computing the DSC, where we considered the manual segmentation as the ground truth

$$DSC = 2 \cdot \frac{|A \cap B|}{|A| + |B|} \quad (3)$$

Furthermore, for each patient and eye region, we computed the mean distance error between the patient ground truth surface and the automatic segmentation result (Fig. 4b). We report the distribution of mean distance error per point across all patients and regions in Figure 5.

The average DSC over all subjects was 94.90 ± 2.12% for the sclera and the cornea, 94.72 ± 1.89% for the VH, and 85.16 ± 4.91% for the lens. Figure 4a summarizes the mean DSC. The mean distance errors were 0.33 ± 0.17 mm for the sclera and cornea, 0.30 ± 0.15 mm for the VH, and 0.17 ± 0.07 mm for the lens (Fig. 4b), with a mean global distribution error of 0.27 ± 0.09 mm per patient. The entire segmentation process took 14 seconds per eye, on average, using Pentium i7 3.4-GHz QuadCore (Intel, Santa Clara, CA) with 8-GB random access memory.

Finally, we applied our segmentation to 2 patients with retinoblastoma. In these cases, the model was robust in detecting the presence of tumors, even when these tumors were large (Fig. 6). We obtained a DSC overlap of 94%, 93.98%, and 92.37% on average for sclera plus cornea, VH, and lens, respectively.

Discussion

The present work describes a method for automatic segmentation of MRI of the eyes based on 3D ASM. Our approach is, to the best of our knowledge, the first framework for automatic extraction of the eye shape with dedicated regions of the sclera, the cornea, the VH, and the lens in the MRI.

We have demonstrated that our model enables accurate segmentation of the eye, with an average error for all ROIs always under the minimum resolution threshold (0.399 mm) and never reaching more than 1.2 mm (Table E1; available online at www.redjournal.org). The results highlight an accurate fit for the posterior part of the VH, where the macula and optic disc are located (Fig. 5a). Furthermore, we noticed a bias toward oversegmentation errors in the frontal part of the eye (Fig. 5b and c). This situation caused the lens to yield a lower average DSC (85.16%) than other regions. The results can be explained due to the small size of the lens in contrast to that of the sclera and VH. This limitation of the DSC index for small regions was already reported by several authors in the field (29, 30).

Within the dataset, we identified an outlier (Table E1; available online at www.redjournal.org, subject 7 [Sub07]) that presented the lowest accuracy during segmentation across all ROIs. This was due to the small size of the eye (the youngest patient, 4 months of age), which made him not well represented by our model. In the future, a larger dataset with greater number of younger patients (<6 months) would address this issue. Furthermore, we also observed that Sub03, Sub14, and Sub15 performed below average during the lens fitting. Nevertheless, there was a general trend toward robust segmentation of the sclera, cornea, and VH, even in cases with a strong variation in eye axial lengths. The final outcome was that lenses in eyes whose size are closer to the mean shape size are

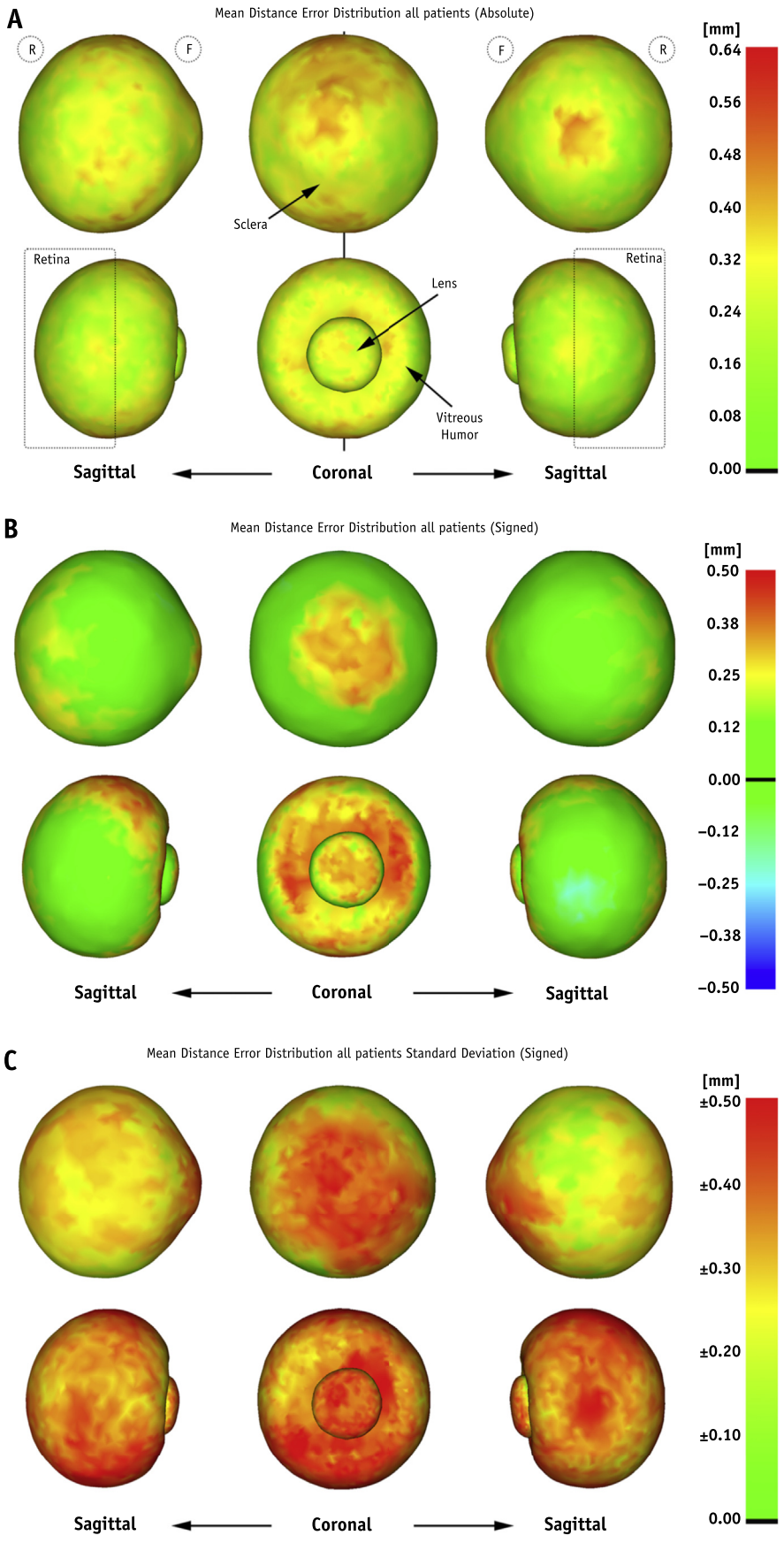

Fig. 5. Mean distance error distribution with respect to the manual segmentation. (A) Unsigned and (B and C) signed distance error to display bias toward over- or undersegmentation.

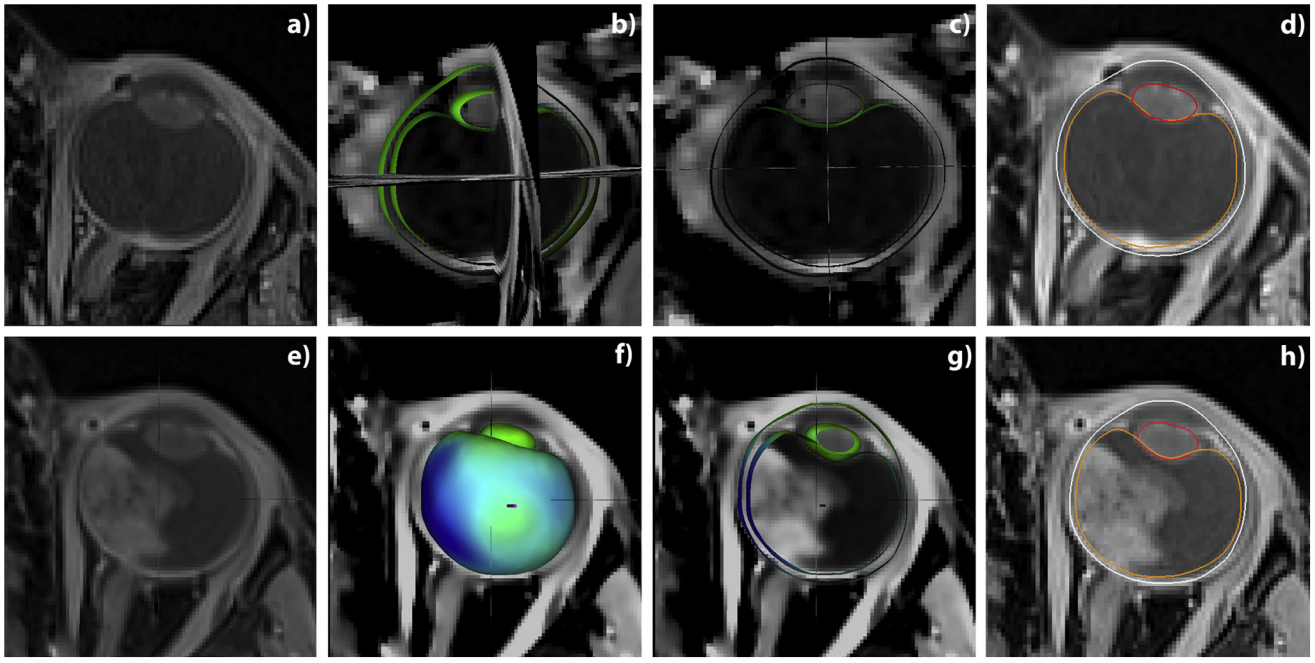

Fig. 6. Patients with retinoblastoma (a and e). Automatic eye segmentation of a small tumor present in the retina (b, c, and d). Robust fit of the vitreous humor and lens for a large tumor (f, g, and h).

better segmented than extreme-sized eyes (Table E2; available online at www.redjournal.org).

Our work demonstrates a novel application of statistical modeling techniques to treatment planning and diagnosis confirmation of intraocular tumors, such as retinoblastoma. The speed, robustness, and reliability of the present method are evidence that it can accommodate the variability existing in the size of eyes (22), as well as solving minor eye orientation issues during the fitting process. Similar to the presented children's eye model and pathological eyes, our framework can be directly applied to create a model for adults, for instance, for delineation of uveal melanoma prior to therapy planning. Uveal melanoma presents an MR Imaging condition very similar to that of retinoblastoma; therefore, leveraging the current framework to adult eye pathology could be the next step.

Conclusions

Although previous works have attempted to delineate or characterize MRI of eyes using a manual qualitative evaluation (14), we are the first to report quantitative results of the segmentation accuracy of MRI. The procedures that we used can provide the basis for objective assessment of the quality of the model fitting in the eye MRI, as it did in other image modalities such as CT (10). Furthermore, the robustness of the model during the segmentation of pathological MRI volumes indicates an important and promising step toward facilitated treatment planning and tumor extent follow-up. A higher MRI diagnostic accuracy for retinoblastoma, particularly for detection of prelaminar optic nerve and choroidal invasion, is crucial for designing effective treatment strategies. Thus our future work will focus on quantitative evaluation in larger datasets.

To our knowledge, this framework is the most accurate and robust tool yet to fully and automatically segment the lens, sclera, cornea, and VH regions in MRI. The approach provides a solution for reducing the time spent in delineating the eye shape and is likely to advance current ocular tumor treatment planning and diagnosis techniques.

References

1. Devesa SS. The incidence of retinoblastoma. *Am J Ophthalmol* 1975; 80:263-265.
2. Balmer A, Zografos L, Munier F. Diagnosis and current management of retinoblastoma. *Oncogene* 2006;25:5341-5349.
3. De Graaf P, Göricke S, Rodjan F, et al. Guidelines for imaging retinoblastoma: Imaging principles and MRI standardization. *Pediatr Radiol* 2012;42:2-14.
4. Munier FL, Verwey J, Pica A, et al. New developments in external beam radiotherapy for retinoblastoma: From lens to normal tissue-sparing techniques. *Clin Experiment Ophthalmol* 2008;36:78-89.
5. De Jong MC, de Graaf P, Noij DP, et al. Diagnostic performance of magnetic resonance imaging and computed tomography for advanced retinoblastoma: A systematic review and meta-analysis. *Ophthalmology* 2014;121:1109-1118.
6. de Graaf P, Barkhof F, Moll AC, et al. Retinoblastoma: MR imaging parameters in detection of tumor extent. *Radiology* 2005;235:197-207.
7. Fanea L, Fagan AJ. Review: Magnetic resonance imaging techniques in ophthalmology. *Mol Vis* 2012;18:2538-2560. Available at: http://www.pubmedcentral.nih.gov/articlerender.fcgi?artid=3482169&tool=pmcentrez&rendertype=abstract. Accessed May 4, 2015.
8. Cuadra MB, Gorthi S, Karahanoglu FI, et al. Model-Based Segmentation and Fusion of 3D Computed Tomography and 3D Ultrasound of the Eye for Radiotherapy Planning. In: Tavares JMRS, Natal Jorge

RM. Computational Vision and Medical Image Processing. Springer: Netherlands; 2011.
9. Galluzzi P, Hadjistilianou T, Cerase A, et al. Is CT still useful in the study protocol of retinoblastoma? *AJNR Am J Neuroradiol* 2009;30:1760-1765.
10. Rüegsegger MB, Cuadra MB, Pica A, et al. Statistical modeling of the eye for multimodal treatment planning for external beam radiation therapy of intraocular tumors. *Int J Radiat Oncol Biol Phys* 2012;84:e541-e547.
11. Beenakker J-WM, Shamonin DP, Webb AG, et al. Automated retinal topographic maps measured with magnetic resonance imaging. *Invest Ophthalmol Vis Sci* 2015;56:1033-1039.
12. Goitein M, Miller T. Planning proton therapy of the eye. *Med Phys* 1983;10:275-283.
13. Dobler B, Bendl R. Precise modelling of the eye for proton therapy of intra-ocular tumours. *Phys Med Biol* 2002;47:593-613.
14. Singh KD, Logan NS, Gilmartin B. Three-dimensional modeling of the human eye based on magnetic resonance imaging. *Invest Ophthalmol Vis Sci* 2006;47:2272-2279.
15. Cootes TF, Taylor CJ, Cooper DH, et al. Active shape models—Their training and application. *Comput Vis Image Underst* 1995;61:38-59.
16. Heimann T, Meinzer HP. Statistical shape models for 3D medical image segmentation: A review. *Med Image Anal* 2009;13:543-563.
17. Lindner C, Thiagarajah S, Wilkinson JM, et al. Fully automatic segmentation of the proximal femur using random forest regression voting. *IEEE Trans Med Imaging* 2013;32:1462-1472.
18. Fritscher KD, Peroni M, Zaffino P, et al. Automatic segmentation of head and neck CT images for radiotherapy treatment planning using multiple atlases, statistical appearance models, and geodesic active contours: Automatic segmentation of head and neck CT images for radiotherapy treatment planning. *Med Phys* 2014;41:051910.
19. Maan B, van der Heijden F. Prostate MR image segmentation using 3D active appearance models. In: PRostate MR Image SEgmentation. Nice, France: PROMISE; 2012, October 1, 2012. p. 44-51.
20. Frangi AF, Rueckert D, Schnabel JA, et al. Automatic construction of multiple-object three-dimensional statistical shape models: Application to cardiac modeling. *IEEE Trans Med Imaging* 2002;21:1151-1166.
21. Wetzel SG, Johnson G, Tan AG, et al. Imaging of the brain with a volumetric interpolated examination. *AJNR Am J Neuroradiol* 2002;23:995-1002.
22. Fledelius HC, Christensen AC. Reappraisal of the human ocular growth curve in fetal life, infancy, and early childhood. *Br J Ophthalmol* 1996;80:918-921.
23. De Zanet SI, Ciller C, Rudolph T, et al. Landmark detection for fusion of fundus and MRI toward a patient-specific multimodal eye model. *IEEE Trans Biomed Eng* 2015;62:532-540.
24. Vercauteren T, Pennec X, Perchant A, et al. Diffeomorphic demons: Efficient non-parametric image registration. *Neuroimage* 2009;45(Suppl 1):S61-S72.
25. Lorensen WE, Cline HE. Marching cubes: A high resolution 3D surface construction algorithm. *SIGGRAPH Comput Graph* 1987;21:163-169.
26. Jolliffe I. Principal Component Analysis. *Wiley StatsRef: Statistics Reference Online* 2014; http://dx.doi.org/10.1002/9781118445112.stat06472.
27. Nyúl LG, Udupa JK. On standardizing the MR image intensity scale. *Magn Reson Med* 1999;42:1072-1081.
28. Vogel H. A better way to construct the sunflower head. *Math Biosci* 1979;44:179-189.
29. Peroni M, Spadea MF, Riboldi M, et al. Validation of automatic contour propagation for 4D treatment planning using multiple metrics. *Technol Cancer Res Treat* 2013;12:501-510.
30. Rohlfing T. Image similarity and tissue overlaps as surrogates for image registration accuracy: Widely used but unreliable. *IEEE Trans Med Imaging* 2012;31:153-163.